PHYSICAL REVIEW B **103**, 235201 (2021)

Editors' Suggestion

Closing of the induced gap in a hybrid superconductor-semiconductor nanowire

D. Puglia,[1,2] E. A. Martinez,[1] G. C. Ménard,[1] A. Pöschl,[1] S. Gronin,[3] G. C. Gardner,[3] R. Kallaher,[3] M. J. Manfra,[3,4,5,6] C. M. Marcus,[1] A. P. Higginbotham,[1,2,*] and L. Casparis[1,†]

[1] *Microsoft Quantum Labs Copenhagen and Center for Quantum Devices, Niels Bohr Institute, University of Copenhagen, Universitetsparken 5, 2100 Copenhagen, Denmark*
[2] *Institute of Science and Technology Austria, Am Campus 1, 3400 Klosterneuburg, Austria*
[3] *Microsoft Quantum Purdue, and Birck Nanotechnology Center, Purdue University, West Lafayette, Indiana 47907, USA*
[4] *Department of Physics and Astronomy, Purdue University, West Lafayette, Indiana 47907, USA*
[5] *School of Materials Engineering, Purdue University, West Lafayette, Indiana 47907, USA*
[6] *School of Electrical and Computer Engineering, Purdue University, West Lafayette, Indiana 47907, USA*

(Received 24 August 2020; revised 20 April 2021; accepted 14 May 2021; published 8 June 2021)

We present conductance-matrix measurements in long, three-terminal hybrid superconductor-semiconductor nanowires, and compare with theoretical predictions of a magnetic-field-driven, topological quantum phase transition. By examining the nonlocal conductance, we identify the closure of the excitation gap in the bulk of the semiconductor before the emergence of zero-bias peaks, ruling out spurious gap-closure signatures from localized states. We observe that after the gap closes, nonlocal signals and zero-bias peaks fluctuate strongly at both ends, inconsistent with a simple picture of clean topological superconductivity.

DOI: 10.1103/PhysRevB.103.235201

I. INTRODUCTION

Hybrid superconductor-semiconductor nanowires are predicted to undergo a field-induced phase transition from a trivial to a topological superconductor, marked by the closure and reopening of the bulk excitation gap, followed by the emergence of Majorana bound states at the nanowire ends [1–3]. Many local density-of-states measurements have reported signatures of Majorana bound states [4], however, this interpretation has been challenged by alternative explanations. A prominent explanation considered in the literature is the emergence of zero-bias peaks before the closure of the induced gap due to smooth confining potentials at the nanowire ends [5–12], and several experiments have found evidence of these effects [13–15]. Since such signatures are expected before the closure of the bulk gap, positively identifying the gap closure is central to reliably identifying topological Majorana zero modes.

The closure of the gap has been studied using tunneling-conductance measurements [16–20], which by design probe the gap locally at the nanowire ends. This approach has given varying evidence on the closure and reopening the gap, with possible theoretical explanations such as weak coupling of bulk states to end probes [21,22], finite-size effects [23], contributions from intrinsic Andreev bound states [24], or contributions from end-localized Andreev bound states [6,7]. More recently, arrays of tunnel probes have been used to gain spatial information on the gap closure [25], while the role of local bound states at the tunnel probe remains an open question.

Reference [26] proposes using the nonlocal conductance as a noninvasive probe of the bulk gap. In particular, one expects that a nonlocal Andreev rectification should generically occur when the bulk gap closes, and that this cannot be mimicked by trivial, localized bound states. In previous work, we performed conductance-matrix measurements on nanowires grown by chemical beam epitaxy, observing sharp bound states that emerged without a gap-closure signature, consistent with the presence of spatially localized Andreev bound states [27,28].

Here, we report measurements on a different set of materials grown by molecular beam epitaxy. We observe field-driven nonlocal Andreev rectification, unambiguously signaling the closure of the bulk excitation gap. We find that the gap generically closes prior to the emergence of zero-bias peaks, which is inconsistent with quasi-Majorana scenarios where zero-bias peaks occur due to end states with a trivially gapped bulk. We do not find evidence of the gap reopening, suggesting the relevance of disorder in the nanowire bulk [8,29].

Over narrow regions of gate voltage, we identify end-to-end correlated zero-bias peaks, explicitly demonstrating that such features occur in the absence of an observable excitation gap. This work demonstrates the use of nonlocal conductance to separate out the contribution between bulk and trivial end features in Majorana wires, and indicates a need for further improvement of bulk material properties in order to firmly establish the existence of Majorana modes.

II. DEVICE AND MEASUREMENT SETUP

We investigate long, three-terminal superconductor-semiconductor hybrid devices shown in Fig. 1(a). InAs nanowires are grown by molecular beam epitaxy with the selective area growth (SAG) method [30–32]. The field-effect mobility of those nanowires without aluminum

---

[*] andrew.higginbotham@ist.ac.at

[†] lucas.casparis@microsoft.com

©2021 American Physical Society

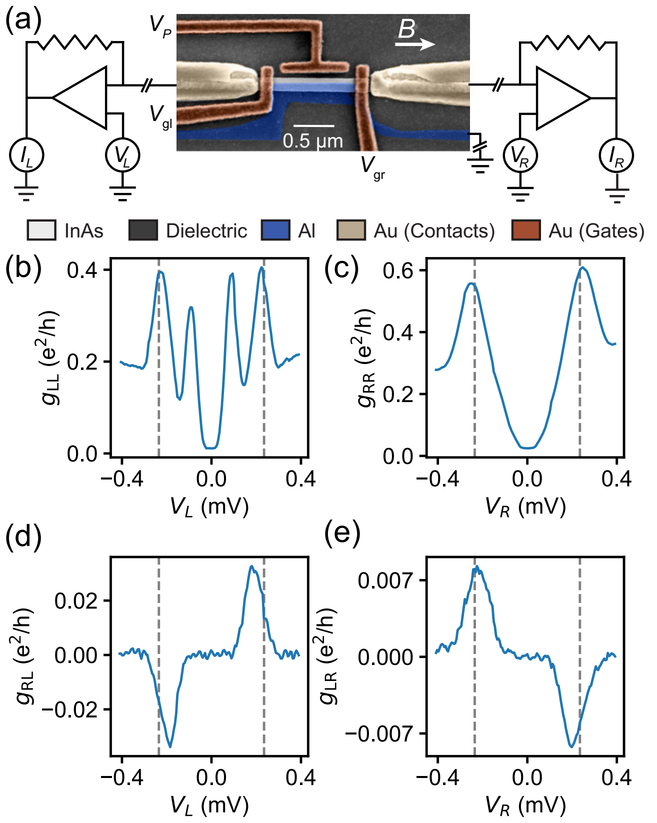

FIG. 1. (a) Schematic of the measurement setup (outer) with a false-color scanning electron microscope image of the device (inner). Plunger gate V_p, tunnel barrier gates V_{gl}, V_{gr}, bias voltages V_L, V_R, and measured currents I_L, I_R are labeled. Line interruptions indicate the in-line filtering of the measurement setup. Direction of applied magnetic field B is indicated by the white arrow. Bias spectroscopy at $B = 0$ for the full conductance matrix: (b) g_{LL}, (c) g_{RR}, (d) g_{RL}, and (e) g_{LR}. Dashed lines are a guide to the eye at ±0.235 mV.

is $\sim 1500\,\mathrm{cm}^2/(\mathrm{Vs})$, similar to vertically grown Al/InAs nanowires which have been studied extensively in other work [18,33]. A 9-nm layer of Al is epitaxially deposited directionally on only one side of the nanowire *in situ* to promote a transparent interface between the superconductor and the semiconductor [34,35]. Following growth, Al is selectively removed from the ends of the wire and the substrate, forming a superconducting terminal which extends from the nanowire to the bond pad. A Ti/Au Ohmic contact is deposited at each end of the wire. Following a global HfOx dielectric deposition, electrostatic Ti/Au gates are deposited. The hybrid segment is $\sim 1\ \mu$m long for the data presented in the main text; data for a $\sim 2\ \mu$m long device, yielding similar results, is presented in Appendix D. The samples were measured in a dilution refrigerator with base temperature $T \sim 50$ mK. The resistance of the dilution refrigerator lines is ~ 1.8 kΩ and typical contact resistance for the SAG devices is 0.5–1 kΩ.

As indicated in Fig. 1(a), the superconducting Al lead is grounded during all measurements. Electrostatic gates V_{gl} and V_{gr} are adjusted to form tunnel barriers between the nanowire and the normal-conducting leads. The tunnel-barrier resistances are tuned to be much larger than the combined resistances of filters, contacts, and amplifier inputs. This tuning ensures that voltage-divider effects are small (see Appendix C for more details); no voltage-divider effects are numerically corrected after the measurement.

A plunger gate V_p is used to tune the chemical potential in the nanowire. The left (right) normal lead is biased with voltage V_L (V_R) while measuring both currents I_L and I_R [27]. Lock-in amplifiers are used to measure local differential conductance on the left $g_{\mathrm{LL}} = dI_L/dV_L$ and right $g_{\mathrm{RR}} = dI_R/dV_R$, as well as the differential nonlocal conductance $g_{\mathrm{LR}} = dI_L/dV_R$ and $g_{\mathrm{RL}} = dI_R/dV_L$. The setup allows the 2×2 conductance matrix

$$g = \begin{bmatrix} g_{\mathrm{LL}} & g_{\mathrm{LR}} \\ g_{\mathrm{RL}} & g_{\mathrm{RR}} \end{bmatrix} \tag{1}$$

to be measured. We emphasize that in this work nonlocal conductance refers simply to off-diagonal terms in this matrix, and is not a statement about nonlocality of Majorana modes. Traces are acquired by sweeping V_L with V_R grounded, and then by sweeping V_R with V_L grounded. Voltage offsets are corrected for by both measuring DC currents and also making sure symmetric features like zero-field coherence peaks appear at the same bias values. A constant voltage offset is assumed for two-dimensional scans.

An example of the bias dependence of g at zero magnetic field is shown in Figs. 1(b)–1(e). In this instance, local conductance measurements on the left and right sides are qualitatively different [Figs. 1(b) and 1(c)]. Both local measurements have suppressed conductance at low bias and exhibit a pair of peaks near $V_{\mathrm{L,R}} \sim \pm 0.24$ mV (dashed vertical line), consistent with coherence peaks originating from the Bardeen-Cooper-Schrieffer (BCS) density of states in the hybrid wire. However, only g_{LL} exhibits an additional pair of peaks at lower bias voltage. The additional peaks in g_{LL} indicate an Andreev bound state on the left side of the device, which is common in superconductor-semiconductor nanowires [16,18], and can generate false-positive Majorana signatures [5–9,11,12].

In contrast to the local conductance, the two nonlocal conductances are qualitatively similar to each other [Figs. 1(d) and 1(e)]. Both nonlocal conductances are negligibly small at low bias, consistent with the presence of an induced gap in the nanowire. As bias is increased from zero, nonlocal conductance dramatically increases once a threshold bias is reached, characteristic of the presence of spatially extended modes above an induced gap. The nonlocal conductance eventually reaches a peak, which roughly aligns with peaks in the local conductance, confirming the identification of an induced gap $\Delta_{\mathrm{ind}} \sim 0.24$ meV. At an even higher bias, the nonlocal conductance becomes negligibly small as expected due to the absorption of quasiparticles in the superconducting lead above the bulk Al gap Δ_{Al} [26]. The disappearance of nonlocal conductance at Δ_{Al} occurs close to the peak in nonlocal conductance at Δ_{ind}, suggesting $\Delta_{\mathrm{ind}} \sim \Delta_{\mathrm{Al}}$, as expected for a transparent, epitaxially matched Al/InAs interface [34–37]. The observed antisymmetric structure of the nonlocal conductance is in theory due to a combination of direct electron transfer and crossed Andreev reflection, and is consistent with numerical simulations including disorder effects [26].

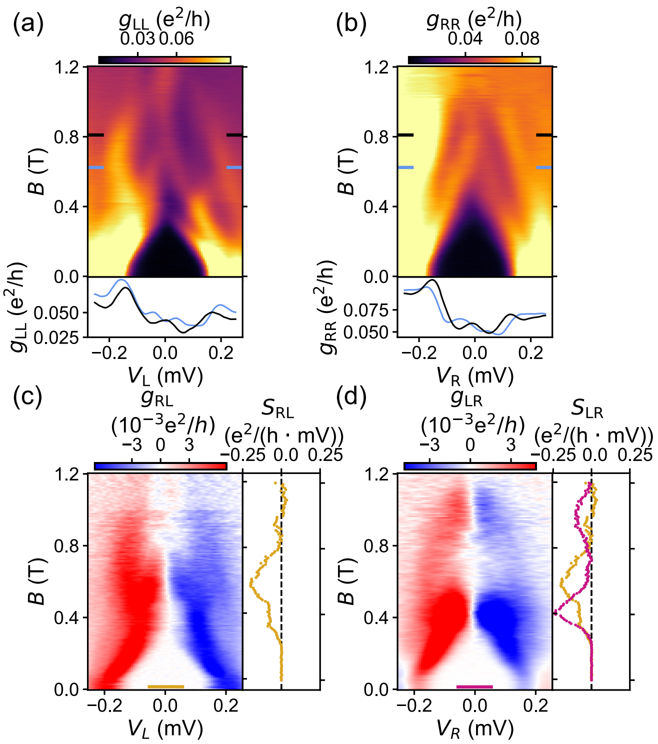

FIG. 2. Local conductances (a) g_{LL} and (b) g_{RR} measured as a function of bias voltage and magnetic field B, with line cuts at $B =$ 0.62 and 0.81 T shown in the bottom panels. Nonlocal conductances (c) g_{RL} and (d) g_{LR} with nonlocal slope S shown in right panel. S was numerically computed over the bias window illustrated by the colored bar in (c) and (d). For comparison, S_{LR} from (c) (orange) is overlaid in (d). Data are taken at $V_p = -1.35$ V.

Unlike the local measurement, the nonlocal signal does not show signatures of the subgap Andreev bound state. This is consistent with the expectation that nonlocal conductance is insensitive to the complicating effects of localized Andreev bound states for devices longer than the induced superconducting coherence length [26]. Motivated by the observed insensitivity to localized states, we now explore nonlocal conductance near the putative topological phase transition, where the role of localized bound states before the closure of the gap is an unsettled topic.

III. MAGNETIC-FIELD DEPENDENCE OF THE FULL CONDUCTANCE MATRIX

In Fig. 2 the full conductance-matrix data are presented as a function of magnetic field B applied parallel to the nanowire. The tunnel barrier and plunger gate voltages were tuned at finite B to exhibit zero-bias peaks in both local conductances. Subsequently, the tunnel barrier gate voltages were held constant and the magnetic field and the plunger gate were swept. Both local conductances are suppressed at low bias at $B = 0$ T [main panels in Figs. 2(a) and 2(b)], and the size of the gap decreases with increasing magnetic field, eventually vanishing for $B \sim 0.4$ T. At a higher magnetic field, zero-bias peaks in the local conductance emerge on both sides of the device, which has never been reported in long superconductor-semiconductor nanowires to the best of our knowledge [bottom panels of Figs. 2(a) and 2(b)]. Zero-bias peaks in the local conductance at both ends of a device are a long-sought signature of Majorana bound states, which motivates further scrutiny of these features by nonlocal measurements.

In the nonlocal conductance, the gapped region around zero bias narrows as B is increased [Figs. 2(c) and 2(d)]. For sufficiently large magnetic fields ($B \gtrsim 0.4$ T), the nonlocal conductance becomes finite around zero applied bias, and is a predominantly odd function of bias, which is the Andreev rectifier gap-closure signature proposed by Ref. [26]. Our observation of the closure of the induced gap before the emergence of zero-bias peaks is inconsistent with a well-studied scenario involving quasi-Majorana modes that predicts the emergence of zero-bias peaks before the closure of the gap [5–9,26].

Upon further increase of the magnetic field, nonlocal conductance is suppressed at low bias for $B \gtrsim 0.8$ T ($B \gtrsim 0.6$ T) for the left (right) side. As previously mentioned, the nonlocal signal is also suppressed when the bias exceeds Δ_{Al}. The bias at which the signal is suppressed decreases with increasing B and, at $B \gtrsim 1.2$ T, the nonlocal signal mostly vanishes. This behavior is consistent with decreasing $\Delta_{Al}(B)$, for higher magnetic fields.

To further quantify the behavior of the nonlocal conductance at low bias, we introduce the nonlocal slope $S \equiv S_{ab}$, given by $S_{ab} = \frac{d^2 I_a}{dV_b^2}|_{V_b=0}$, for $a = L, R$ and $b = R, L$. S is a metric for the strength of nonlocal conductance, which takes into account the predominantly antisymmetric behavior of the nonlocal conductance in bias, giving $g_{ab} \approx S_{ab} V_b$ at low bias. To extract S, numerical derivatives are computed from a polynomial fit over a bias window of ±61 μV centered around zero bias (see Appendix B).

The right-side panels in Figs. 2(c) and 2(d) show S_{RL} and S_{LR}, numerically extracted from the nonlocal conductances (see Appendix B). For small magnetic fields, S is zero, consistent with the previous qualitative observation that the nonlocal conductance is gapped at low field. S smoothly increases near $B \sim 0.35$ T, initially exhibiting similar behavior on both sides of the device [Fig. 2(d)]. The appearance of gapless nonlocal conductance at a single characteristic field confirms the earlier interpretation of a closure in the induced gap in the entire hybrid wire.

Interestingly, S changes nonmonotonically with B. S_{RL} is small over the interval (0.8 T, 1.2 T), whereas S_{LR} is small over the interval (0.6 T, 0.8 T). Thus, although the induced gap in the nanowire closes at a single characteristic field, S fluctuates unevenly on both sides of the device at large fields and remains sizable on at least one side when zero-bias peaks emerge [Fig. 4(d) right panel].

It is interesting to note that the nonlocal conductances g_{LR} and g_{RL} differ strongly at large magnetic fields. In short devices it was previously found that $g_{LR} \sim g_{RL}$ even for large magnetic fields, indicating spatially homogeneous BCS charge [27]. Following the same interpretation in the current device, the difference between g_{LR} and g_{RL} indicates a spatial inhomogeneity of the BCS charge, perhaps attributable to the longer device length or increased disorder [38].

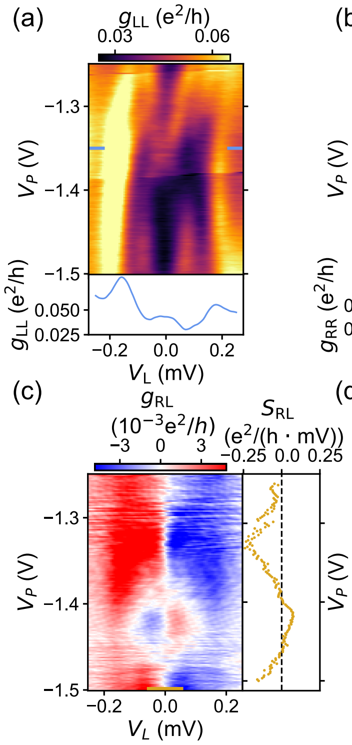

FIG. 3. Local conductances (a) g_{LL} and (b) g_{RR} measured as a function of bias voltage and plunger gate, with line cuts at $V_p = -1.35$ V shown in the bottom panels. Nonlocal conductances (c) g_{RL} and (d) g_{LR} with nonlocal slope S shown in right panel. S was numerically computed over the bias window illustrated by the colored bar in (c) and (d). For comparison, S_{RL} from (c) (orange) is overlaid in (d). Data taken at $B = 0.7$ T.

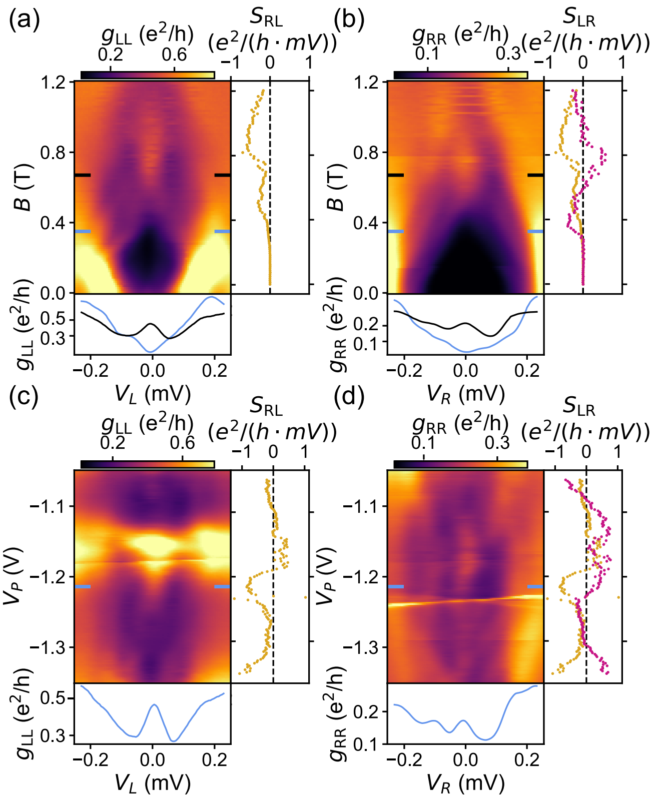

FIG. 4. Local conductances (a) g_{LL} and (b) g_{RR} measured as a function of magnetic field and bias voltage with $V_p = -1.2$ V. Line cuts taken at $B = 0.32$ and 0.64 T and the bottom panels, and nonlocal conductance amplitude S in the right panels. Local conductances (c) g_{LL} and (d) g_{RR} measured as a function of gate voltage and bias voltage with $B = 0.7$ T. Line cuts taken at $V_p = 1.21$ V on the bottom panels, and nonlocal slope S on the right panels. For comparison, S_{RL} from (c) (orange) is overlaid in (d).

IV. GATE-VOLTAGE DEPENDENCE OF THE FULL CONDUCTANCE MATRIX

The gate-voltage dependence of the zero-bias peaks and nonlocal conductance provides further information on the origin of these features. Figure 3 shows full conductance-matrix measurements as a function of plunger gate voltage. The scan was acquired by setting the magnetic field to 0.7 T, which is slightly lower than the value at which zero-bias peaks emerge in Figs. 2(a) and 2(b) [line cuts in the bottom panel in Figs. 3(a)nd 3(b)], and then sweeping the plunger gate. In Fig. 3(a), we see the state on the left side crosses through zero bias, which is not expected for a Majorana bound state. The state on the right side of the wire, however, remains robust to voltage changes of over 100 mV [Fig. 3(b)]. The overall dependence of the left and right zero-bias peaks on gate voltage is qualitatively different, which is not consistent with a pair of Majorana bound states in a clean topological superconductor.

Throughout the gate-voltage sweep, the nonlocal conductance fluctuates strongly, changing sign several times while remaining predominantly antisymmetric in bias voltage [Figs. 3(c) and 3(d)]. There is no apparent correlation between sign changes in the nonlocal conductance on either side. Further, the low-bias nonlocal response persists even in the absence of zero-bias peaks. Changing the plunger-gate by several volts does not remove the nonlocal conductance (see Sec. VI), indicating that the presence of spatially extended modes is more robust than zero-bias peaks.

Summarizing, the data in Figs. 2 and 3 are characterized by the generic emergence of fluctuating, low-bias nonlocal conductance above a characteristic field, and zero-bias peaks that are not end-to-end correlated. The experimentally identified apparent gapless regime would be consistent with theoretical explanations where a gap exists but is immeasurably small, or where the characteristic length scales for subgap states exceed the device sizes we have studied (1–2 μm). These observations do not fit neatly within a known picture of a clean topological superconductor since the uncorrelated behavior of zero-bias peaks and lack of a gap reopening is inconsistent with a pair of Majorana bound states at the ends of the wire, however, theoretical studies including disorder have suggested that gapless high-field behavior can emerge [26,29].

V. FULL CONDUCTANCE MATRIX WITH ZERO-BIAS PEAKS ON BOTH SIDES

Figure 4 shows a different data set, taken over a nearby plunger region but with different tunnel-barrier voltages. As magnetic field is increased, the gap in the local conductance

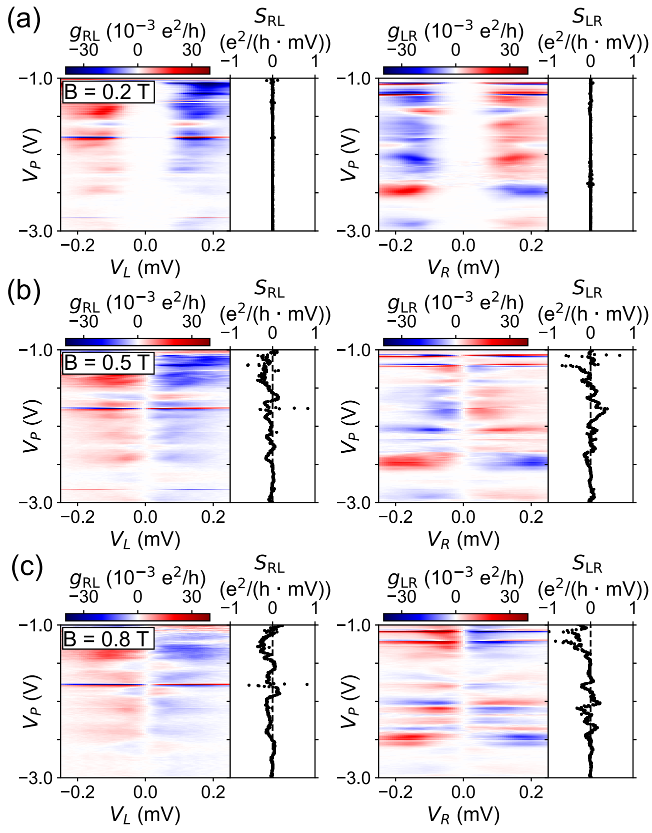

FIG. 5. Nonlocal conductances g_{RL} and g_{LR} measured as a function of bias voltage and plunger gate V_P taken at $B = 0.2$ T for (a), $B = 0.5$ T for (b), and $B = 0.8$ T for (c). The nonlocal slope S is shown in the right panel.

is suppressed, and zero-bias peaks emerge on both sides of the device for an extended range in magnetic fields [Figs. 4(a) and 4(b), line cuts in bottom panels]. The nonlocal slope S increases before the zero-bias peaks emerge, remaining sizable for large magnetic fields, qualitatively similar to the data set in Fig. 2.

Figures 4(c) and 4(d) present plunger-gate scans taken at $B = 0.7$ T, which is slightly after the emergence of zero-bias peaks in the local conductance. In both cases, low-bias peaks can be seen in line cuts [bottom panels in Figs. 4(c) and 4(d)], and remain near zero bias for over 100 mV plunger gate. A strong, bias-independent increase in conductance is seen in Fig. 4(c) at approximately $V_p = -1.15$ V, which is compatible with resonant transmission due to coupling through a local state. The zero-bias peak does not split when it crosses this feature, suggesting that it is not coupled to the local state [18,39]. The gate dependence of the zero-bias peaks on both sides is qualitatively similar, hinting that this particular zero-bias peak could be due to a single extended mode. We emphasize that, in the absence of an excitation gap, spatially extended modes are not necessarily of a topological origin. Further, we have established in previous work that in the presence of a dense, low-energy spectrum, statistically significant correlations can occur even in the presence of a topologically trivial excitation gap [28].

VI. ROBUST BEHAVIOR OF THE GAPPED AND GAPLESS REGIMES

The preceding sections have shown that a regime with low-bias nonlocal conductance extends over large ranges of magnetic field and several hundreds of millivolts in gate voltage, persisting even when zero-bias peaks are absent. The robustness of this regime is further demonstrated in Fig. 5, where nonlocal conductance is plotted as a function of V_p and $V_{L,R}$ at three different magnetic fields. The plunger gate voltage V_p is varied over its full range, limited by undesired increases (decreases) to the tunnel couplings at positive (negative) V_p due to cross coupling. At small fields, nonlocal conductance is only observed above a characteristic bias scale, which we operationally identify as the induced gap [Fig. 5(a)]. At higher field the nonlocal response is observed for low biases, although the sign and magnitude fluctuates strongly [Figs. 5(b) and 5(c)]. The nonlocal response persists for the entire range of several volts in plunger-gate voltage, which greatly exceeds the range over which zero-bias peaks are stable (cf. Fig. 4). Thus, low-bias nonlocal response is a large-scale feature of the data set, and is substantially more robust than zero-bias peaks.

Figure 6 shows the local conductances for the same magnetic fields and plunger range. At $B = 0.2$ T, sub-gap features showing up only in one local conductance [Fig. 6(a)] are not present in the nonlocal conductance [Fig. 5(a)], consistent with the expectation that nonlocal conductance is insensitive to low-energy localized states when the rest of the wire is still trivially gapped. At higher magnetic fields there is a dense structure of low-bias peaks [Figs. 6(b) and 6(c)], with no obvious correlation to the nonlocal data.

VII. CONCLUSIONS

Based on these observations, which have been reproduced in over 10 devices (see Appendix D for similar measurements in a ∼2-μm-long device), we conclude that the emergence of spatially extended states above a critical field, and a proliferation of zero-bias peaks, is a generic feature of our devices. Theoretical studies of nonlocal conductance in our geometry have shown that gapless high-field behavior can result from disorder effects [26,29], which may explain the current observations. It is interesting to note that the field-effect mobility of our SAG is comparable to the widely studied vertically grown nanowires [16,18,33], so it is possible that a gapless regime could exist in those systems as well.

In our previous work [27], where we studied the magnetic-field dependence of short nanowires grown by chemical beam epitaxy (CBE), we observed many sharp subgap states at low field, and did not observe a nonlocal gap-closure signature at high field. In addition, the inferred charge of low-energy states did not have the magnetic field dependence expected for Majorana zero modes [27,38]. We speculate that the CBE-grown SAG wires we studied in Ref. [27] are described by a standard quasi-Majorana scenario where zero-bias peaks emerge with a gapped bulk, in contrast to the current MBE-grown SAG wires where zero-bias peaks are associated with a gapless, disordered bulk. Three-terminal studies of SAG wires have thus revealed two operating regime in Majorana

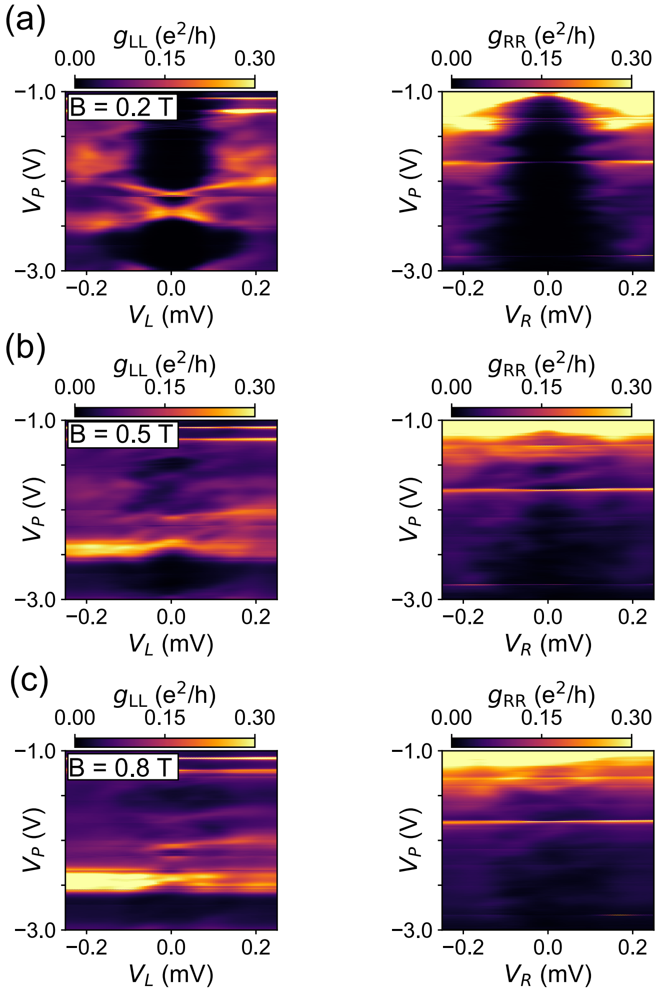

FIG. 6. Local conductances $g_{\rm LL}$ and $g_{\rm RR}$ measured as a function of bias voltage and plunger gate V_P taken at $B = 0.2$ T for (a), $B = 0.5$ T for (b), and $B = 0.8$ T for (c). Data were taken simultaneously with nonlocal measurements in Fig. 5.

wires: a quasi-Majorana regime with localized end states, and a gapless regime with a disordered bulk. It is an interesting topic for future work to determine if similar observations hold in other systems that can be cleanly contacted with a third lead, such as full-shell nanowires [15] or two-dimensional electron gases [20].

We experimentally demonstrated that full conductance-matrix measurements are capable of excluding two widely considered scenarios in hybrid one-dimensional systems: localized zero-energy states emerging before the gap closes and clean topological superconductivity. Localized zero-energy states emerging before the gap closes is inconsistent with our observation that apparently gapless nonlocal conductance generically precedes the appearance of peaks in local conductance. Clean topological superconductivity is excluded by the lack of end-to-end correlations and the absence of a gap reopening signature. Based on comparison with the theoretical literature [8,29], we have suggested that the gapless regime is associated with a disordered bulk. Since the lack of an excitation gap prohibits any progress on the path to topological quantum computation, we anticipate that nonlocal measurements will play an important role in benchmarking candidate systems for topological quantum computation.

Note added in proof. Recently, we became aware of related work that measures zero-bias peaks on both ends of a hybrid nanowire, but does not report the nonlocal conductance measurements [40].

ACKNOWLEDGMENTS

We acknowledge insightful discussions with K. Flensberg, E. B. Hansen, T. Karzig, R. Lutchyn, D. Pikulin, E. Prada, and R. Aguado. This work was supported by Microsoft Project Q and the Danmarks Grundforskningsfond. C.M.M. acknowledges support from the Villum Fonden.

A.P.H. and L.C. contributed equally to this work.

APPENDIX A: TUNNEL BARRIER SCANS

Figure 7 shows the dependence of the local conductances $g_{\rm LL}$ and $g_{\rm RR}$ on the left and right tunnel barriers at a magnetic field $B = 0.7$ T. The conductance data are normalized to the high-bias values $g^N_{\rm LL} = g_{\rm LL}(220\,\mu{\rm V})$ for every cutter gate voltage. This is done to allow for comparison of the data in a large range of conductance values. $g^N_{\rm LL}$ ranges from $\sim 1.2\,\frac{e^2}{h}$ to pinch off in Fig. 7(a). $g^N_{\rm RR}$ ranges from $\sim 0.8\,\frac{e^2}{h}$ to pinch off in Fig. 7(d). Local conductance on the left and right show many resonances as function of tunnel gate [Figs. 7(a) and 7(d)].

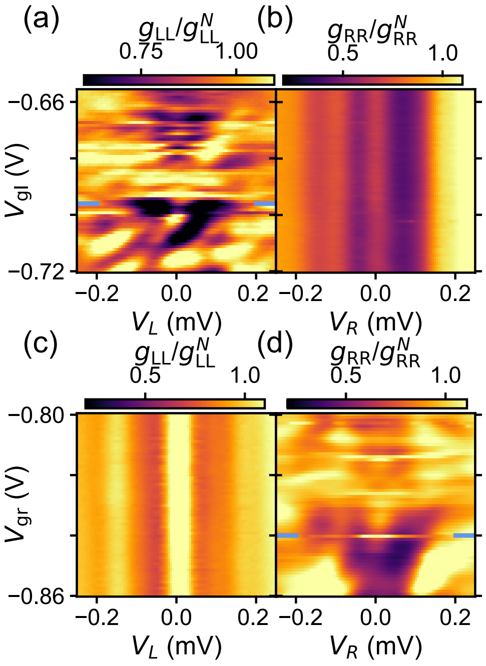

FIG. 7. Tunnel-barrier dependence of local conductance at $B = 0.7$ T. (a) [(b)] Local conductance $g_{\rm LL}$ ($g_{\rm RR}$) normalized by conductance at high bias $g^N_{\rm LL}$ ($g^N_{\rm RR}$) measured as a function of bias voltage and left tunnel-barrier $V_{\rm gl}$, while $V_{\rm gr} = -0.84$ V. (c) [(d)] $g_{\rm LL}$ ($g_{\rm RR}$) normalized by conductance at high bias $g^N_{\rm LL}$ ($g^N_{\rm RR}$) as a function of bias and right tunnel barrier $V_{\rm gr}$, while $V_{\rm gl} = -0.696$ V. The blue markers indicate the tunnel-barrier values for the field and plunger dependence presented in Fig. 4 in Sec. V, $V_{\rm gl} = -0.696$ V and $V_{\rm gr} = -0.84$ V.

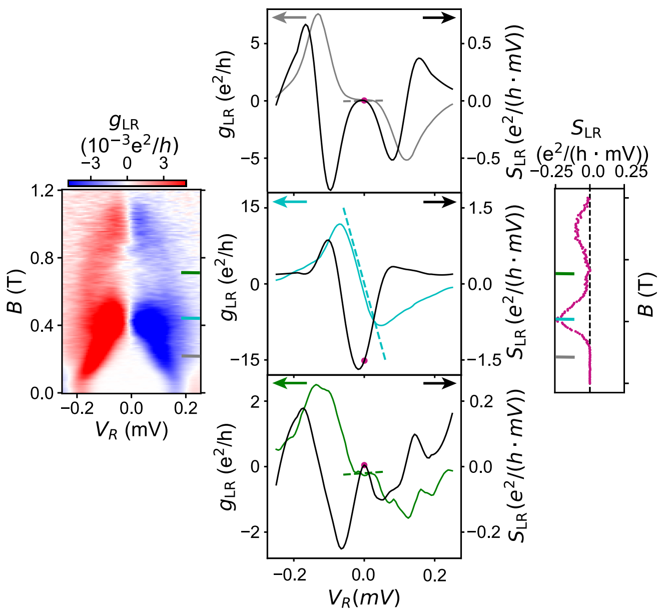

FIG. 8. Slope extraction from nonlocal conductance. The left panels shows the g_{LR} field scan introduced in Fig. 2(d) in Sec. III. The center panels present how the nonlocal slope S_{LR} was extracted for three values of field: 0.2 T (gray), 0.41 T (blue), and 0.71 T (green). The line cut of g_{LR} is shown by a continuous colored line for the respective fields. The first derivative of the line cut (S_{LR}) was calculated by the Savitzky-Golay filter and is shown in black with the zero-bias values evidenced by a magenta dot. For reference, the value of the slope at zero bias was multiplied by the bias voltage and displayed as a color dashed line for each line cut. The right panel presents the slope S_{LR} extracted at zero bias (magenta dot in the center panel) for the entire field scan.

Zero-bias peaks appear frequently, and are typically present for a few tens of millivolts of gate voltage. We note that the local conductance on the side with constant gate voltage is not affected [Figs. 7(b) and 7(c)] by the barrier change on the other side. This observation is consistent with changing local tunnel coupling to a robust topological phase in the middle of the nanowire, but also with a purely local origin of the zero-bias peaks (ZBPs), highlighting again the need for a technique probing the bulk of the sample.

APPENDIX B: EXTRACTION OF *S*

Figure 8 shows how the slope of the nonlocal conductance S was extracted. The first derivative for every line cut was calculated by a Savitzky-Golay filter over a bias window of $\pm 61\ \mu$V centered around zero bias.

APPENDIX C: VOLTAGE-DIVIDER EFFECTS

The impedance of measurement circuitry, in particular due to the resistance of in-line filters, can cause spurious contributions to conductance measurements. Although these effects are relatively trivial in two-terminal devices, in the three-terminal case the situation is more complicated. We have found exact expressions to correct the conductance matrix for voltage-divider effects, and validated them experimentally [41].

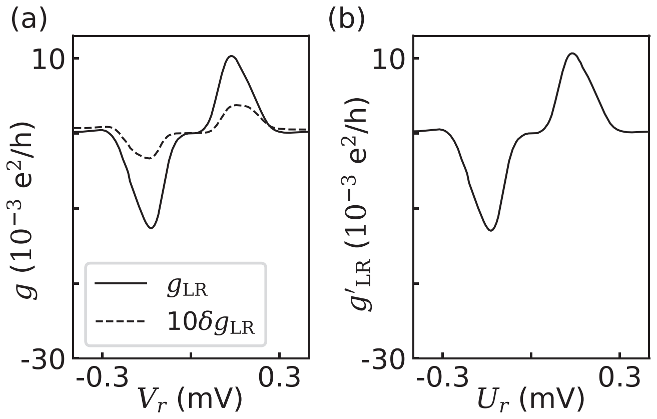

FIG. 9. (a) Nonlocal conductance g_{LR} taken from $V_p = -1.25$ V in Fig. 5(a), and 10 times the voltage-divider correction factor $\delta g_{\mathrm{LR,div}}$ computed from Eq. (C5). (b) Corrected nonlocal conductance g'_{LR} computed from $g'_{\mathrm{LR}} = g_{\mathrm{LR}} + \delta g_{\mathrm{LR}}$.

The goal is to translate the 2×2 conductance matrix $g(V_L, V_R)$ [Eq. (1)], which depends on the voltages V_L, V_R at the top of the cryostat, into a 2×2 conductance matrix

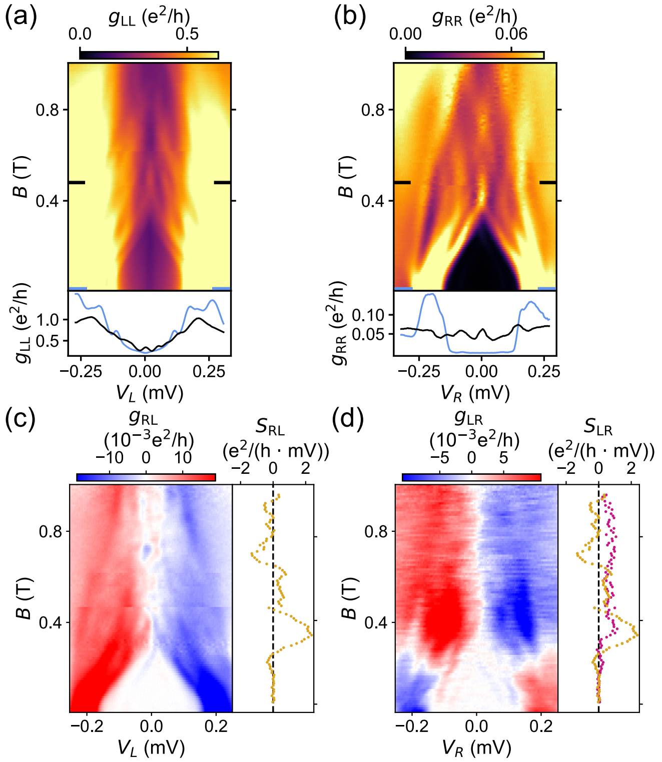

FIG. 10. Magnetic field dependence of the full conductance matrix for a 2-μm-long device. Local conductances (a) g_{LL} and (b) g_{RR} measured as a function of bias voltage and magnetic field B, with line cuts at $B = 0$ and 0.48 T shown in the bottom panels. Nonlocal conductances (c) g_{RL} and (d) g_{LR} with nonlocal conductance slope S shown in right panel. S was numerically computed using the same procedure as detailed in Appendix B. For comparison, S_{LR} from (c) (orange) is overlaid in (d).

$g'(U_L, U_R)$ which depends on the true voltages at the terminals of the device at the bottom of the cryostat. Reference [41] shows that this can be accomplished with the matrix transformation

$$g'(U_L, U_R) = g(V_L, V_R)[\mathbb{I}_2 - \mathbb{Z}g(V_L, V_R)]^{-1}, \tag{C1}$$

where $\mathbb{I}_2$ is the 2×2 identity and $\mathbb{Z}$ is a matrix encoding the line impedances of the devices. For the special case where all three device terminals have the same line impedance Z (as is applicable here), $\mathbb{Z}$ reads as

$$\mathbb{Z} = \begin{bmatrix} 2Z & Z \\ Z & 2Z \end{bmatrix}. \tag{C2}$$

When the line impedance Z is much larger than the resistances associated with the device $Z \gg g_{\mathrm{LL}}, g_{\mathrm{LR}}, g_{\mathrm{RL}}, g_{\mathrm{RR}}$, Eq. (C1) can be expanded in a geometric series to give

$$g'(U_L, U_R) = g(V_L, V_R)[\mathbb{I}_2 + \mathbb{Z}g(V_L, V_r)] \tag{C3}$$

$$= g(V_L, V_R) + \delta g(V_L, V_R), \tag{C4}$$

where in the last line we have introduced the voltage-divider correction matrix $\delta g = g\mathbb{Z}g$.

To explicitly test the importance of the voltage-divider correction, we consider an off-diagonal entry

$$\delta g_{\mathrm{LR}} = g_{\mathrm{LR}}(2g_{\mathrm{LL}} + 2g_{\mathrm{RR}} + g_{\mathrm{LR}})Z + g_{\mathrm{LL}}g_{\mathrm{RR}}Z, \tag{C5}$$

with $Z = 1.83\ \mathrm{k}\Omega$ set from the line resistance of the cryostat. As shown in Fig. 9, the voltage-divider correction is δg_{LR} is more than an order of magnitude smaller than the measured data, and applying the correction makes no qualitative change.

APPENDIX D: EXAMPLE DATA FROM A SECOND DEVICE

Figure 10 shows data from a 2-μm-long three-terminal device. The main features of the data are qualitatively similar to the data shown in the main text for the 1-μm device, namely, the emergence of a robust, low-energy nonlocal conductance above a critical field, as seen from the nonlocal conductance. This particular device exhibited many subgap states at zero field, including the occurrence of ZBPs in both g_{LL} and g_{RR}.

[1] R. M. Lutchyn, J. D. Sau, and S. Das Sarma, Phys. Rev. Lett. **105**, 077001 (2010).

[2] Y. Oreg, G. Refael, and F. von Oppen, Phys. Rev. Lett. **105**, 177002 (2010).

[3] X.-L. Qi and S.-C. Zhang, Rev. Mod. Phys. **83**, 1057 (2011).

[4] R. M. Lutchyn, E. P. A. M. Bakkers, L. P. Kouwenhoven, P. Krogstrup, C. M. Marcus, and Y. Oreg, Nat. Rev. Mater. **3**, 52 (2018).

[5] G. Kells, D. Meidan, and P. W. Brouwer, Phys. Rev. B **86**, 100503(R) (2012).

[6] E. Prada, P. San-Jose, and R. Aguado, Phys. Rev. B **86**, 180503(R) (2012).

[7] C.-X. Liu, J. D. Sau, T. D. Stanescu, and S. Das Sarma, Phys. Rev. B **96**, 075161 (2017).

[8] A. Vuik, B. Nijholt, A. R. Akhmerov, and M. Wimmer, SciPost Phys. **7**, 61 (2019).

[9] C. Reeg, O. Dmytruk, D. Chevallier, D. Loss, and J. Klinovaja, Phys. Rev. B **98**, 245407 (2018).

[10] F. Peñaranda, R. Aguado, P. San-Jose, and E. Prada, Phys. Rev. B **98**, 235406 (2018).

[11] J. Avila, F. Peñaranda, E. Prada, P. San-Jose, and R. Aguado, Commun. Phys. **2**, 133 (2019).

[12] E. Prada, P. San-Jose, M. W. A. de Moor, A. Geresdi, E. J. H. Lee, J. Klinovaja, D. Loss, J. Nygård, R. Aguado, and L. P. Kouwenhoven, Nat. Rev. Phys. **2**, 575 (2020).

[13] E. J. H. Lee, X. Jiang, R. Aguado, G. Katsaros, C. M. Lieber, and S. De Franceschi, Phys. Rev. Lett. **109**, 186802 (2012).

[14] P. Yu, J. Chen, M. Gomanko, G. Badawy, E. P. A. M. Bakkers, K. Zuo, V. Mourik, and S. M. Frolov, Nat. Phys. **17**, 482 (2021).

[15] M. Valentini, F. Peñaranda, A. Hofmann, M. Brauns, R. Hauschild, P. Krogstrup, P. San-Jose, E. Prada, R. Aguado, and G. Katsaros, arXiv:2008.02348.

[16] V. Mourik, K. Zuo, S. M. Frolov, S. R. Plissard, E. P. A. M. Bakkers, and L. P. Kouwenhoven, Science **336**, 1003 (2012).

[17] A. Das, Y. Ronen, Y. Most, Y. Oreg, M. Heiblum, and H. Shtrikman, Nat. Phys. **8**, 887 (2012).

[18] M. T. Deng, S. Vaitiekėnas, E. B. Hansen, J. Danon, M. Leijnse, K. Flensberg, J. Nygård, P. Krogstrup, and C. M. Marcus, Science **354**, 1557 (2016).

[19] S. Vaitiekėnas, M.-T. Deng, J. Nygård, P. Krogstrup, and C.M. Marcus, Phys. Rev. Lett. **121**, 037703 (2018).

[20] F. Nichele, A. C. C. Drachmann, A. M. Whiticar, E. C. T. O'Farrell, H. J. Suominen, A. Fornieri, T. Wang, G. C. Gardner, C. Thomas, A. T. Hatke, P. Krogstrup, M. J. Manfra, K. Flensberg, and C. M. Marcus, Phys. Rev. Lett. **119**, 136803 (2017).

[21] T. D. Stanescu, S. Tewari, J. D. Sau, and S. Das Sarma, Phys. Rev. Lett. **109**, 266402 (2012).

[22] D. Rainis, L. Trifunovic, J. Klinovaja, and D. Loss, Phys. Rev. B **87**, 024515 (2013).

[23] R. V. Mishmash, D. Aasen, A. P. Higginbotham, and J. Alicea, Phys. Rev. B **93**, 245404 (2016).

[24] Y. Huang, H. Pan, C.-X. Liu, J. D. Sau, T. D. Stanescu, and S. Das Sarma, Phys. Rev. B **98**, 144511 (2018).

[25] A. Grivnin, E. Bor, M. Heiblum, Y. Oreg, and H. Shtrikman, Nat. Commun. **10**, 1940 (2019).

[26] T. O. Rosdahl, A. Vuik, M. Kjaergaard, and A. R. Akhmerov, Phys. Rev. B **97**, 045421 (2018).

[27] G. C. Ménard, G. L. R. Anselmetti, E. A. Martinez, D. Puglia, F. K. Malinowski, J. S. Lee, S. Choi, M. Pendharkar, C. J. Palmstrøm, K. Flensberg, C. M. Marcus, L. Casparis, and A. P. Higginbotham, Phys. Rev. Lett. **124**, 036802 (2020).

[28] G. L. R. Anselmetti, E. A. Martinez, G. C. Ménard, D. Puglia, F. K. Malinowski, J. S. Lee, S. Choi, M. Pendharkar, C. J. Palmstrøm, C. M. Marcus, L. Casparis, and A. P. Higginbotham, Phys. Rev. B **100**, 205412 (2019).

[29] H. Pan, J. D. Sau, and S. Das Sarma, Phys. Rev. B **103**, 014513 (2021).

[30] S. Vaitiekėnas, A. M. Whiticar, M.-T. Deng, F. Krizek, J. E. Sestoft, C. J. Palmstrøm, S. Marti-Sanchez, J. Arbiol, P. Krogstrup, L. Casparis, and C. M. Marcus, Phys. Rev. Lett. **121**, 147701 (2018).

[31] F. Krizek, J. E. Sestoft, P. Aseev, S. Marti-Sanchez, S. Vaitiekėnas, L. Casparis, S. A. Khan, Y. Liu, T. Stankevič, A. M. Whiticar, A. Fursina, F. Boekhout, R. Koops, E. Uccelli, L. P. Kouwenhoven, C. M. Marcus, J. Arbiol, and P. Krogstrup, Phys. Rev. Mater. **2**, 093401 (2018).

[32] J. S. Lee, S. Choi, M. Pendharkar, D. J. Pennachio, B. Markman, M. Seas, S. Koelling, M. A. Verheijen, L. Casparis, K. D. Petersson, I. Petkovic, V. Schaller, M. J. W. Rodwell, C. M. Marcus, P. Krogstrup, L. P. Kouwenhoven, E. P. A. M. Bakkers, and C. J. Palmstrøm, Phys. Rev. Mater. **3**, 084606 (2019).

[33] S. M. Albrecht, A. P. Higginbotham, M. Madsen, F. Kuemmeth, T. S. Jespersen, J. Nygård, P. Krogstrup, and C. M. Marcus, Nature (London) **531**, 206 (2016).

[34] P. Krogstrup, N. L. B. Ziino, W. Chang, S. M. Albrecht, M. H. Madsen, E. Johnson, J. Nygård, C. M. Marcus, and T. S. Jespersen, Nat. Mater. **14**, 400 (2015).

[35] W. Chang, S. M. Albrecht, T. S. Jespersen, F. Kuemmeth, P. Krogstrup, J. Nygård, and C. M. Marcus, Nat. Nanotechnol. **10**, 232 (2015).

[36] A. E. G. Mikkelsen, P. Kotetes, P. Krogstrup, and K. Flensberg, Phys. Rev. X **8**, 031040 (2018).

[37] A. E. Antipov, A. Bargerbos, G. W. Winkler, B. Bauer, E. Rossi, and R. M. Lutchyn, Phys. Rev. X **8**, 031041 (2018).

[38] J. Danon, A. B. Hellenes, E. B. Hansen, L. Casparis, A. P. Higginbotham, and K. Flensberg, Phys. Rev. Lett. **124**, 036801 (2020).

[39] M.-T. Deng, S. Vaitiekėnas, E. Prada, P. San-Jose, J. Nygård, P. Krogstrup, R. Aguado, and C. M. Marcus, Phys. Rev. B **98**, 085125 (2018).

[40] S. Heedt, M. Quintero-Pérez, F. Borsoi, A. Fursina, N. van Loo, G. P. Mazur, M. P. Nowak, M. Ammerlaan, K. Li, S. Korneychuk, J. Shen, M. A. Y. van de Poll, G. Badawy, S. Gazibegovic, K. van Hoogdalem, E. P. A. M. Bakkers, and L. P. Kouwenhoven, arXiv:2007.14383.

[41] E. A. Martinez, A. Pöschl, E. B. Hansen, M. A. Y. van de Poll, S. Vaitiekėnas, A. P. Higginbotham, and L. Casparis, arXiv:2104.02671.